Natural Resources Canada | Ressources naturelles Canada

**GEOLOGICAL SURVEY OF CANADA**
**OPEN FILE 9289e**

# Electromagnetic mapping of sublacustrine saline permafrost, Rankin Inlet, Nunavut

**G.A. Oldenborger**

**2026**

Canada

**GEOLOGICAL SURVEY OF CANADA**
**OPEN FILE 9289e**

# Electromagnetic mapping of sublacustrine saline permafrost, Rankin Inlet, Nunavut

**G.A. Oldenborger**

**2026**



**Recommended citation**
Oldenborger, G.A., 2026. Electromagnetic mapping of sublacustrine saline permafrost, Rankin Inlet, Nunavut; Geological Survey of Canada, Open File 9289e, 22 p., https://doi.org/10.4095/pqunx9q1bk

Publications in this series have not been edited; they are released as submitted by the author.

ISSN 2816-7155
ISBN 978-0-660-78397-0
Catalogue No. M183-2/9289E-PDF
https://doi.org/10.4095/pqunx9q1bk

## SUMMARY

An electromagnetic geophysical survey was conducted over First Landing Lake in the vicinity of Rankin Inlet, Nunavut as part of a study on lake taliks. Survey results show areas of high electrical conductivity associated with the shallow lake terrace. High electrical conductivity is interpreted to result from sublacustrine saline permafrost. Saline permafrost will have a direct influence on permafrost dynamics and lake talik formation.

# Table of Contents

SUMMARY ..... i
INTRODUCTION ..... 1
STUDY AREA ..... 1
METHODS ..... 2
RESULTS ..... 4
DISCUSSION ..... 5
CONCLUSION ..... 5
REFERENCES ..... 7
APPENDIX A ..... 17

## INTRODUCTION

This Open File reports on the occurrence of sublacustrine saline permafrost detected by a frequency-domain electromagnetic (FEM) survey conducted over First Landing Lake in the vicinity of Rankin Inlet, Nunavut. The geophysical survey was conducted with the primary objective of testing the suitability of FEM methods for mapping occurrence of bottom-fast ice (BFI) and frozen substrate as part of a larger study on lake taliks (LeBlanc et al., 2021, LeBlanc et al., 2022; Sladen et al., 2024). For the Rankin Inlet region, BFI is expected for water depths less than the average ice thickness of 1.7 m and permafrost is expected for water depths less than 1.1 m for which the duration of ice-substrate contact is long enough to sustain subzero mean annual temperature (LeBlanc et al., 2024). In contrast, floating ice, unfrozen water, and taliks are expected for large lakes and deeper water. However, many large lakes exhibit shallow terraces that can influence lake taliks. FEM surveys can provide non-invasive information on ice and permafrost conditions.

Geophysical methods that are sensitive to electrical conductivity, such as FEM surveys, can be useful for permafrost studies due to the strong dependence of electrical conductivity on the phase change of water to ice (e.g., Herring et al., 2023). In general, BFI with frozen substrate will be less conductive than BFI with unfrozen substrate or non-BFI with unfrozen water and substrate. Surveys performed near the time of maximum ice thickness may be used to infer occurrence of BFI, frozen substrate, and talik potential.

## STUDY AREA

The Hamlet of Rankin Inlet is located on the western coast of Hudson Bay in the Kivalliq Region of Nunavut, Canada (Figure 1). Rankin Inlet is within the continuous permafrost zone where 90–100% of the land area is underlain by permafrost (Heginbottom et al., 1995). Mean annual ground temperature at the top of permafrost varies from −9.5 to −5.5°C and active layer thickness ranges from 60 to 160 cm (LeBlanc and Oldenborger, 2021). First Landing Lake is located approximately 7 km northwest of the Hamlet of Rankin Inlet. The lake has an approximate volume of $4.2\times10^6$ $m^3$ with a maximum depth of 17.6 m (Budkewitsch et al., 2011). Bedrock beneath the lake is largely volcanic with sedimentary rocks crossing the centre of the lake in the east-west direction (Golder Associates Ltd., 2021). The surrounding surficial geology is marine, glacial, and glaciofluvial with bedrock cliffs on the southern shore (McMartin, 2002). First Landing Lake is large enough and deep enough to support a talik (LeBlanc et al., 2021). However, it exhibits a terrace extending several hundred meters into the lake from the northern shoreline (Figure 1) which may influence talik formation.

## METHODS

Frequency-domain electromagnetic surveys involve the measurement of the in-phase and quadrature secondary magnetic field strengths resulting from a fixed loop-loop sensor configuration (e.g., Huang and Fraser, 2001). The measurements are sensitive to electrical conductivity, dielectric permittivity, and magnetic permeability of the subsurface (e.g, Hanssens et al., 2019b). Ground-based FEM instruments are typically operated in a configuration whereby the quadrature response is predominantly a function of the electrical conductivity (McNeil, 1980). The in-phase response is often unstable (e.g., Delefortrie et al., 2014) and is typically ignored, along with the effects of dielectric permittivity, and magnetic permeability.

### Data Acquisition

Ice- and ground-based FEM data were collected over First Landing Lake on April 28, 2024 at the approximate time of maximum ice thickness. The study area and survey track are shown in Figure 1. The survey site was selected based on the presence of a large lake terrace that may influence talik occurrence (LeBlanc et al., 2022). Site conditions were snow-covered lake ice and tundra shorelines with an air temperature of approximately −10°C during data acquisition.

Data were collected using a DualEM-42 sensor (Taylor, 1999). The DualEM-42 has two sets of horizontal co-planer (HCP) and perpendicular (PRP) coil pairs fixed at 2.0/2.1 m and 4/4.1 m separation, operating at a frequency of 9 kHz (Figure 2a). Nominal depths of investigation are 1 m (PRP2), 2 m, (PRP4), 3 m (HCP2) and 6 m (HCP4). Measurements consist of four channels of apparent conductivity (mS/m) and in-phase response (ppt), along with sensor pitch, roll, temperature, and voltage.

The DualEM sensor was mounted on a sled at 0.14 m height (Figure 2b) and data were collected at walking speed at a sample rate of 1 Hz with synchronous collection of GNSS position data. The in-phase data were observed to be unstable and are not considered further. The survey was conducted as multiple acquisitions starting from and ending at a fixed reference point (Figure 1). At a nearby ice survey location, snow depth, ice thickness, and water depth were measured as 0.4 m, 1.3 m, and 5.1 m from ice surface (Figure 1). Electrical conductivity of the lake water at the ice survey location 5 m below ice surface was 20 mS/m at 1.5°C.

### Processing and Inversion

The data processing flow consists of position synchronization, drift corrections, static calibration, filtering, and spatial averaging of apparent conductivity followed by inversion of the processed data for electrical conductivity. No temperature compensation is considered and the data represent the conditions at in-situ temperatures (i.e., Oldenborger et al., 2020; Oldenborger, 2021).

Position synchronization involves assigning geographic coordinates acquired from an external GNSS receiver to every data sample, based on comparison to time stamps from the internal sensor GNSS receiver that is used for signal timing. The same position was assigned to all four sensor channels, although there is a 1 m offset between the 2 m and 4 m coil pair centres (Figure 2a). Synchronization is accurate to 0.5 s and no temporal averaging occurs given the 1 Hz sampling rates for both the DualEM sensor and GNSS receiver.

Drift correction attempts to account for variations in sensor measurements that arise due to changes in temperature, voltage, and other factors. Channel-by channel drift was calculated based on comparison of the first and last 30 s of data for every acquisition. Drift correction was applied using a channel-specific time-based linear compensation. Drift was observed to be less than 1 mS/m per hour for all channels; HCP4 was the most stable channel with drift less than 0.01 mS/m per hour.

Calibration (or levelling) is used to account for channel specific offsets and differences at the reference point between the different acquisitions. The power supply, data logger, and GNSS receiver are known to cause offsets in apparent conductivity, most significantly for the PRP2 and HCP2 channels, and negligibly for the HCP4 channel. Offsets were not measured for the field configuration. In the absence of direct measurements of offset, a channel-by channel calibration was calculated for each acquisition by correcting the data at the reference point to match synthetic data simulated using the full electromagnetic solution for a reference model (Hanssens et al., 2019b).

The reference model is based on measurements from the nearby ice survey (Figure 1) and is comprised of two layers: 1.7 m of snow and ice at 1 mS/m over water and substrate at 20 mS/m. The assigned electrical conductivity of the upper layer is representative of dry snow and ice (e.g., Reynolds and Paren, 1984; Mikucki et al., 2015) and is near the low conductivity limit of resolution for the DualEM-42. The lake substrate at the reference point is 5.6 m from the sensor and may influence the calibration. However, the expected bulk electrical conductivity of the unfrozen substrate is similar to the measured lake water conductivity (e.g., Oldenborger et al., 2020; Oldenborger, 2024) and the two-layer reference model accurately reproduces the measured HCP4 apparent conductivity at the reference point, while generally reproducing the measured apparent conductivity for all other channels.

The synthetic modelling establishes a constant set of apparent conductivity values at the reference point to which all acquisitions were levelled:

$[\sigma_{\mathrm{PRP2}}, \sigma_{\mathrm{PRP4}}, \sigma_{\mathrm{HCP2}}, \sigma_{\mathrm{HCP4}},]_{\mathrm{ref}}$ = [3.3 mS/m, 7.2 mS/m 9.0 mS/m, 12.9 mS/m].

This procedure accounts for both offsets due to the power supply and variations between acquisitions. (Note that if offsets were directly measured for the field configuration, reference point levelling might still be required.) The specific corrections are acquisition-dependent, but are approximately 3.5 mS/m, 1.5 mS/m, −3 mS/m, and 0.5 mS/m for the PRP2, PRP4, HCP2, and HCP4 channels. Similar calibrations of FEM data have been implemented that utilize supporting data (e.g., McLachlan et al., 2021). The calibration procedure herein involves an implicit assumption that the reference model is correct and laterally applicable over the footprint of the instrument. An example acquisition is shown in Figure 3 with drift correction and calibration applied.

## RESULTS

Following drift correction and calibration of all acquisitions, the continuous apparent conductivity measurements were averaged over a 10 m by 10 m grid for each channel along with sensor pitch, roll, temperature, and voltage (Figures 4 and 5). Spatial standard deviations were calculated for each channel over every grid cell, along with an average standard deviation for all four apparent conductivity channels. Averages with less than three observations per grid cell were removed. The averaged data have a maximum absolute pitch of 4.3°, a maximum absolute roll of 8.9°, and a maximum average standard deviation of 8.1 mS/m. The average apparent conductivity measurements were then inverted for electrical conductivity as independent soundings for every grid cell according to the method detailed in Appendix A. The result is a collection of 1D electrical conductivity models that are then combined to form a 3D model volume. Individual 1D models with a root-mean-square prediction error (RMSE) greater than 20% were excluded from the 3D model volume. Results of recovered electrical conductivity are shown for both an unconstrained two-layer inversion (Figures 6 and 7), and a smoothness-constrained multi-layer inversion (Figure 8).

Both models fit the data to nearly equivalent degrees ($\phi_d = 1.6$, $\phi_d = 1.5$) and much of the recovered structure is similar. Both models predict a very low conductivity surface consistent with snow over lake ice offshore and snow over a frozen active layer onshore. This very low conductivity surface layer is highly uniform over deep water but is variable in thickness over the terrace and increases in thickness onshore. Below the surface layer, recovered electrical conductivity is low and uniform in deep water (including the reference point). Both models predict a variable region of elevated electrical conductivity corresponding to the lake terrace, and very high electrical conductivity in two distinct regions. The multi-layer inversion predicts a larger zone of high conductivity with the outer regions of the high conductivity zone being at greater depth (Figure 8). Onshore, the electrical conductivity is intermediate in terms of magnitude and uniformity. For the two-layer model, the onshore transition from low to moderate conductivity at depth is necessarily sharp (Figure 7). In contrast, the multi-layer inversion predicts a gradual transition to moderately conductive ground at depth that may be due to the smoothness constraint, but a similar smoothing effect is not observed in deep water (Figure 8).

## DISCUSSION

The observed variations in electrical conductivity over the lake terrace, and particularly the regions of high conductivity are interpreted to result from saline permafrost, and not solely from the distribution of BFI and talik occurrence. Given fresh porewater, BFI with frozen substrate would result in reduced unfrozen water content, and decreased electrical conductivity (e.g., Oldenborger, 2021). This is not observed anywhere on the lake terrace (Figure 6). Electrical conductivity is observed to increase both from the onshore to offshore transition and from the deep water to terrace transition.

At the transition from deep water to the terrace edge, electrical conductivity below the ice layer is observed to be slightly higher than that of the lake water (Figure 6). For unfrozen ground, this result can be explained if the pore fluid conductivity of the substrate is approximately 5–10 times greater than that of the fresh lake water, or 100–200 mS/m. However, electrical conductivity is observed to increase from the terrace edge toward shore, reaching a maximum in excess of 300 mS/m near a known location of BFI (1.3 m thick) at the time of the survey (Figure 6). The existence of BFI alone does not imply permafrost conditions, but elevated electrical conductivity persists towards the shoreline, past the 1 m isobath where permafrost is most likely present.

For unfrozen ground, a bulk electrical conductivity of 300 mS/m would require substrate pore fluid conductivity greater than 100 times that of the fresh lake water, or 2 S/m. Partially frozen ground would require higher pore fluid conductivity to achieve the observed electrical conductivity due to reduced unfrozen water content. In terms of salinity, a fluid conductivity of 2 S/m at 0°C corresponds to approximately 20 g/kg NaCl with a freezing point depression of 1.2°C (e.g., Oldenborger, 2021). The presence of saline permafrost is consistent with postglacial inundation of the land surface in the Kivalliq Region (Dyke, 2004). In the Hamlet of Rankin Inlet, permafrost salinity of 3.0–30.6 ppt (g/kg) has been reported at depths of 2.4–6.1 m (Hivon, 1991).

## CONCLUSION

A frequency-domain electromagnetic (FEM) survey was conducted over First Landing Lake near Rankin Inlet, Nunavut. The recovered two-layer and multi-layer models of electrical conductivity do not conform with a simple conceptual model of variations in electrical conductivity being representative of the spatial distribution of BFI and frozen substrate over the shallow lake terrace. Elevated electrical conductivity is observed to be associated with the lake terrace and is interpreted to result from the presence sublacustrine saline permafrost that complicates interpretation of FEM data in terms of BFI and frozen or unfrozen substrate. Saline permafrost will have a direct influence on permafrost dynamics and talik formation.

ACKNOWLEDGEMENTS

Part of the Natural Resources Canada GEM-GeoNorth Program. Data collected with assistance from C. Duchesne. Ice survey data provide by W. Sladen. Internal review by A.-M. LeBlanc.

## REFERENCES


Budkewitsch, P., Prévost, C., Pavlic, G., Pregitzer, M., 2011. Description of water depth survey datasets from Rankin Inlet, Nunavut. Geological Survey of Canada, Open File 6751. https://doi.org/10.4095/288667

Delefortrie, S., De Smedt, P., Saey, T., Van De Vijver, E., Van Meirvenne, M., 2014. An efficient calibration procedure for correction of drift in EMI survey data. Journal of Applied Geophysics 110, 115–125. https://doi.org/10.1016/j.jappgeo.2014.09.004

Dyke, A.S., 2004. An outline of North American deglaciation with emphasis on central and northern Canada. Developments in Quaternary Sciences 2, 373–424. https://doi.org/10.1016/s1571-0866(04)80209-4

Golder Associates Ltd., 2021. Summary of Hydrogeology Existing Conditions, Meliadine Extension. Report No. 20136436-855-R-ExistingConditionsReport-Rev3, Agnico Eagle Mines Limited.

Hanssens, D., Delefortrie, S., Bobe, C., Hermans, T., De Smedt, P., 2019a. Improving the reliability of soil EC-mapping: Robust apparent electrical conductivity (rECa) estimation in ground-based frequency domain electromagnetics. Geoderma 337, 1155–1163. https://doi.org/10.1016/j.geoderma.2018.11.030

Hanssens, D., Delefortrie, S., De Pue, J., Van Meirvenne, M., De Smedt, P., 2019b. Frequency-domain electromagnetic forward and sensitivity modeling: Practical aspects of modeling a magnetic dipole in a multilayered half-space. IEEE Geoscience and Remote Sensing 7, 74–85. https://doi.org/10.1109/MGRS.2018.2881767

Heginbottom, J.A., Dubreuil, M.H., Harker, P.T., 1995. Canada, Permafrost. National Atlas of Canada, 5th ed., Plate 2.1, MCR 4177.

Herring, T., Lewkowicz, A.G., Hauck, C., Hilbich, C., Mollaret, C., Oldenborger, G.A., Uhlemann, S., Farzamian, M., Calmels, F., Scandroglio, R., 2023. Best practices for using electrical resistivity tomography to investigate permafrost. Permafrost and Periglacial Processes 34, 494–512. https://doi.org/10.1002/ppp.2207

Hivon, E.G., 1991. Behaviour of Saline Frozen Soils (Ph.D.). University of Alberta.

Huang, H., Fraser, D.C., 2001. Mapping of the resistivity, susceptibility, and permittivity of the earth using a helicopter-borne electromagnetic system. Geophysics 66, 148–157. https://doi.org/10.1190/1.1444889

Lagarias, J.C., Reeds, J.A., Wright, M.H., Wright, P.E., 1998. Convergence properties of the Nelder-Mead simplex method in low dimensions. SIAM Journal of Optimization 9, 112–147. https://doi.org/10.1137/S1052623496303470

LeBlanc, A.-M., Chartrand, J., Smith, S.L., 2021. Estimation of maximum lake depth from the surrounding topography: Towards a regional assessment of the occurrence of taliks below Arctic lakes. Geological Survey of Canada, Scientific Presentation 122. https://doi.org/10.4095/328242

LeBlanc, A.-M., Chartrand, J., Smith, S.L., 2022. Regional assessment of the presence of taliks below Arctic lakes, Nunavut. Geological Survey of Canada, Scientific Presentation 138. https://doi.org/10.4095/330205

LeBlanc, A.-M., Oldenborger, G.A., 2021. Ground temperature, active layer thickness and ground ice conditions in the vicinity of Rankin Inlet, Nunavut. Canada-Nunavut Geoscience Office, Summary of Activities 2020, 63–72.

LeBlanc, A-M, Sladen, W.E, Faucher, B., 2024. Lake-bottom temperature on shallow and deep terraces for sublacustrine open talik assessment near Rankin Inlet, Nunavut, Canada. International Conference on Permafrost, 378–379.

McLachlan, P., Blanchy, G., Binley, A., 2021. EMagPy: Open-source standalone software for processing, forward modeling and inversion of electromagnetic induction data. Computers & Geosciences 146, 104561. https://doi.org/10.1016/j.cageo.2020.104561

McMartin, I. 2002. Surficial geology, Rankin Inlet, Nunavut. Geological Survey of Canada, Open File 4116. https://doi.org/10.4095/299616

McNeil, J.D., 1980. Electromagnetic Terrain Conductivity Measurements at Low Induction Numbers. Geonics Ltd., Technical Note TN-6.

Mikucki, J., Auken, E., Tulaczyk, S., Virginia, R.A., Schamper, C., Sørensen, K.I., Doran, P.T., Dugan, H., Foley, N., 2015. Deep groundwater and potential subsurface habitats beneath an Antarctic dry valley. Nature Communications 6, 6831. https://doi.org/10.1038/ncomms7831

Nocedal, J., Wright, S.J., 2006. Numerical Optimization, Second Edition. Springer Series in Operations Research, Springer Verlag.

Oldenborger, G.A., 2021. Subzero temperature dependence of electrical conductivity for permafrost geophysics. Cold Regions Science and Technology 182, 103214. https://doi.org/10.1016/j.coldregions.2020.103214

Oldenborger, G.A., 2024. Time-domain electromagnetic soundings for talik investigations, Rankin Inlet, Nunavut. Geological Survey of Canada, Open File 9170. https://doi.org/10.4095/p60hysa40q

Oldenborger, G.A., Short, N., LeBlanc, A.-M., 2020. Electrical conductivity and ground displacement in permafrost terrain. Journal of Applied Geophysics 181, 104148. https://doi.org/10.1016/j.jappgeo.2020.104148

Reynolds, J., Paren, J., 1984. Electrical resistivity of ice from the Antarctic Peninsula, Antarctica. Journal of Glaciology 30, 289–295. https://doi.org/10.3189/S0022143000006110

Sladen, W.E., LeBlanc, A.-M., Chartrand, J., van der Sanden, J., 2024. Using RADARSAT constellation mission imagery to support talik mapping, Rankin Inlet, Nunavut, Canada. Proceedings of the International Conference on Permafrost, 390–397.

Taylor, R.S., 1999. Development and applications of geometric-sounding electromagnetic (EM) systems, in: SEG Expanded Abstracts. Society of Exploration Geophysicists, pp. 544–547. https://doi.org/10.1190/1.1821076

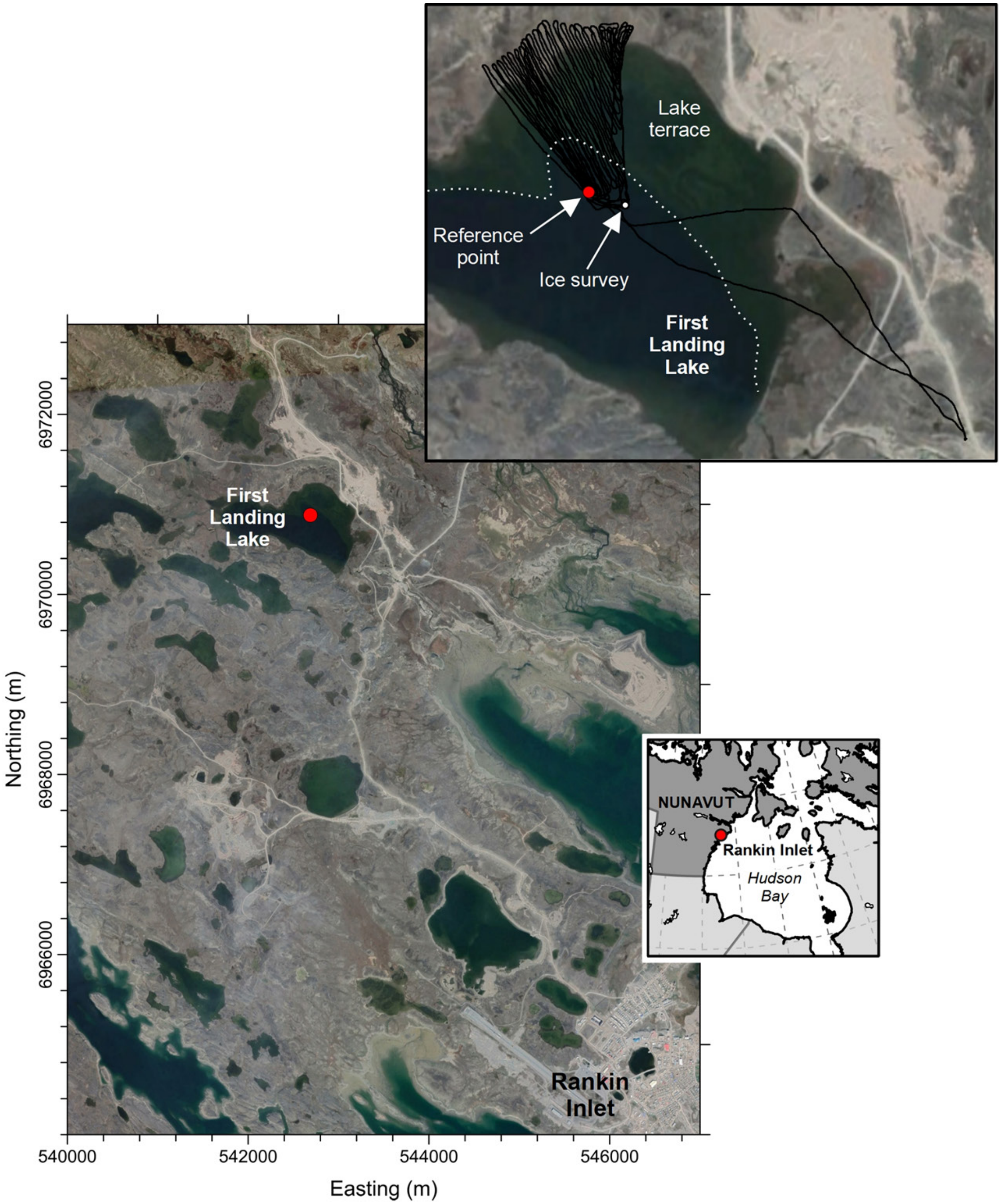


**Figure 1.** First Landing Lake study area near Rankin Inlet, Nunavut. Inset shows the lake survey track over the lake terrace, the reference point (red circle), and the nearby ice survey location (white circle). Coordinates are Easting and Northing, WGS84 UTM Zone 15N. Background image: Google Earth, © 2023 Maxar Technologies, © 2023 TerraMetrics.

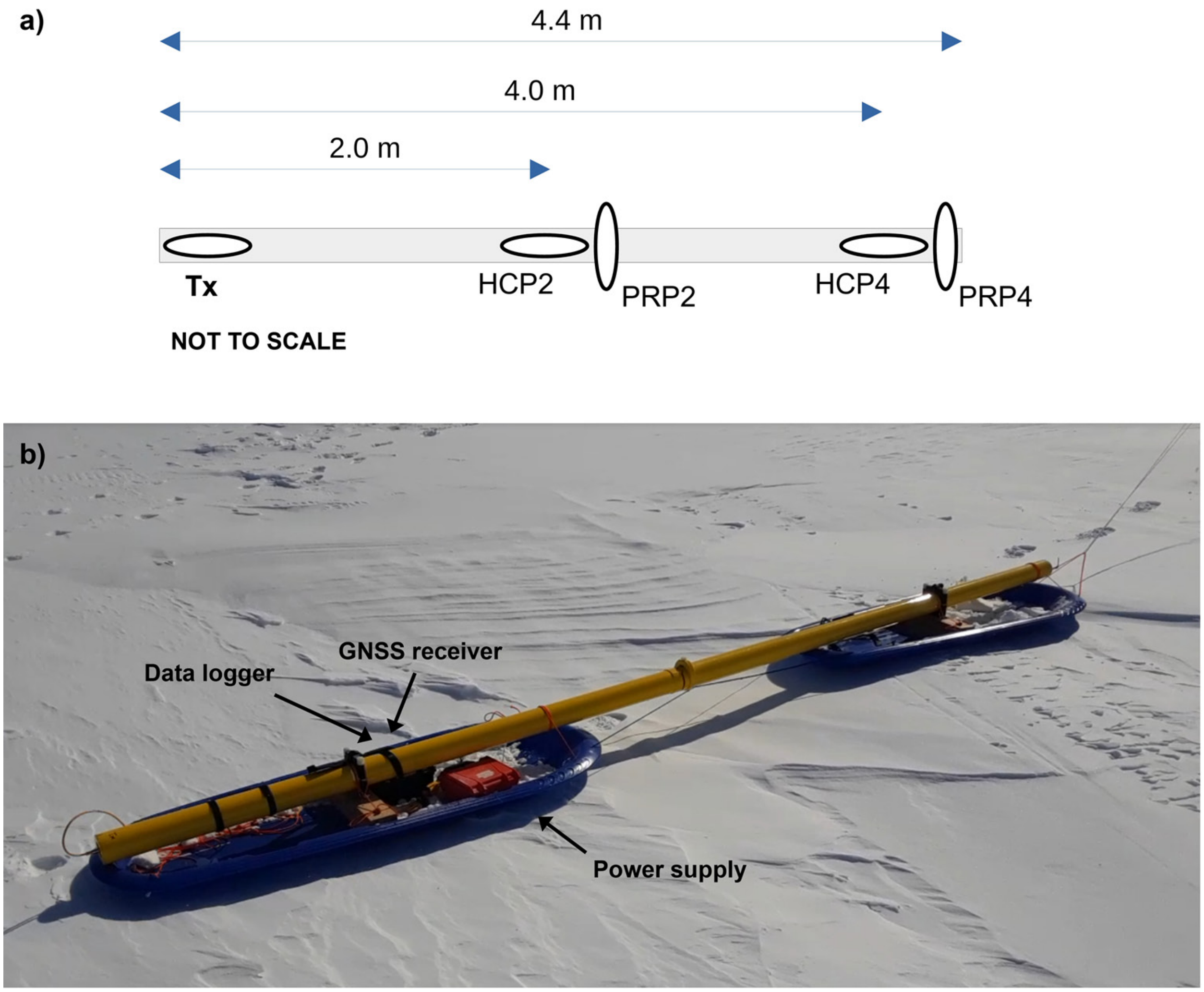


**Figure 2.** a) Schematic of the DualEM-42 sensor configuration with four coil pairs in horizontal co-planar (HCP) and perpendicular (PRP) orientations. b) Sled-based sensor deployment.

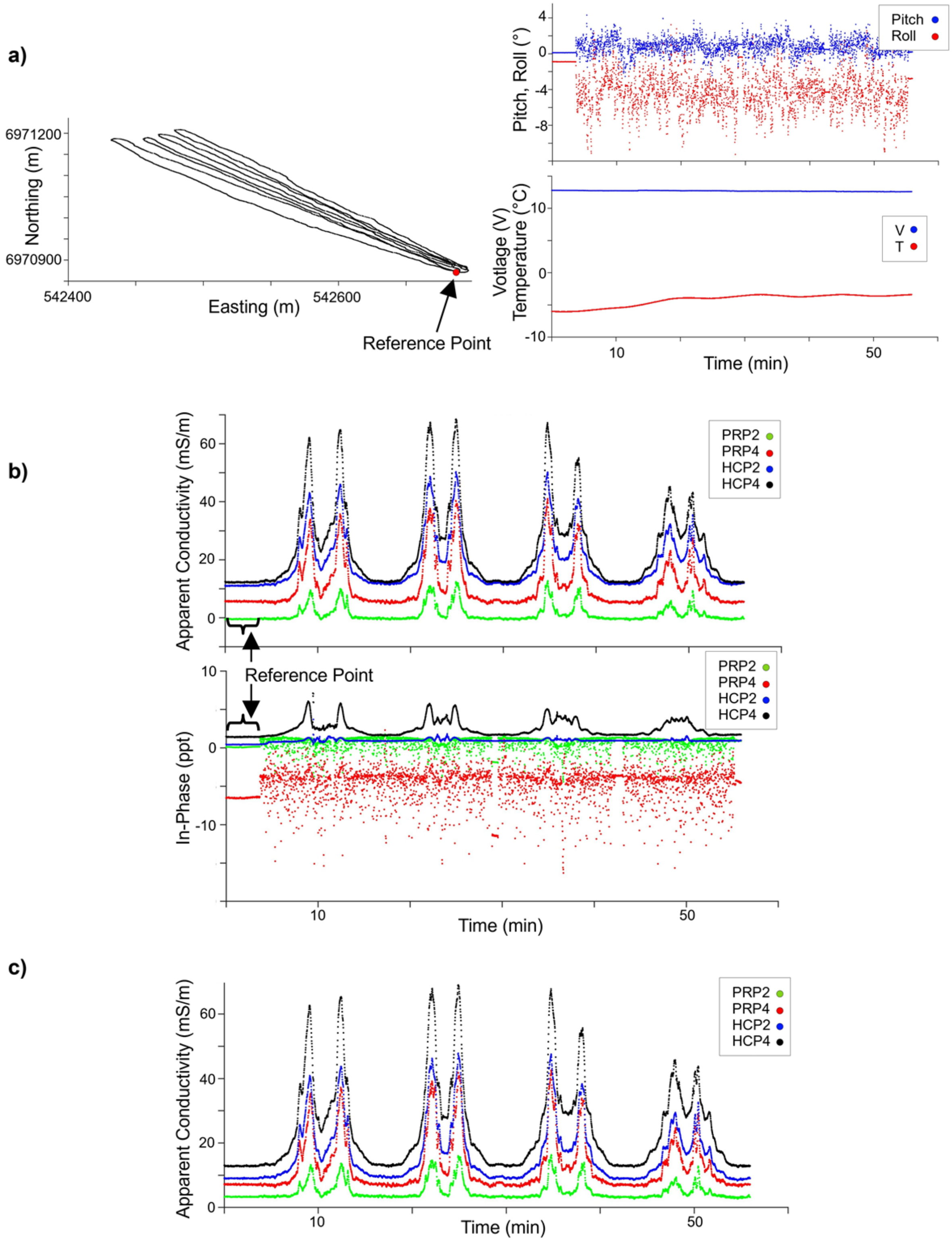


**Figure 3.** Example data acquisition starting and ending at the reference point. a) Survey coordinates, pitch, roll voltage, and temperature. b) Raw apparent conductivity (quadrature) and in-phase data from the four coil pairs. c) Drift-corrected and calibrated apparent conductivity.

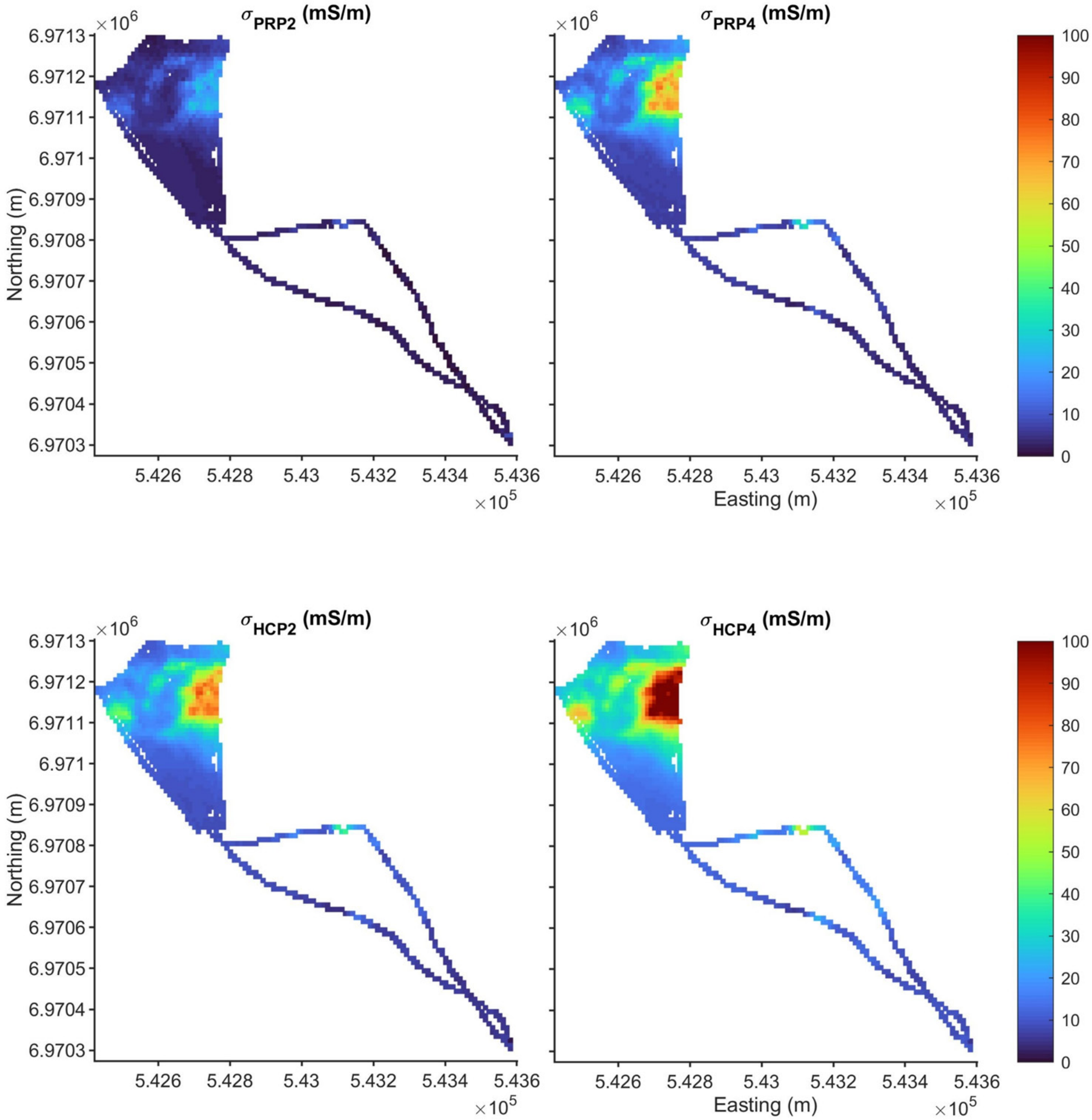


**Figure 4.** Apparent electrical conductivity for the four coil pairs averaged over a 10m by 10m grid.

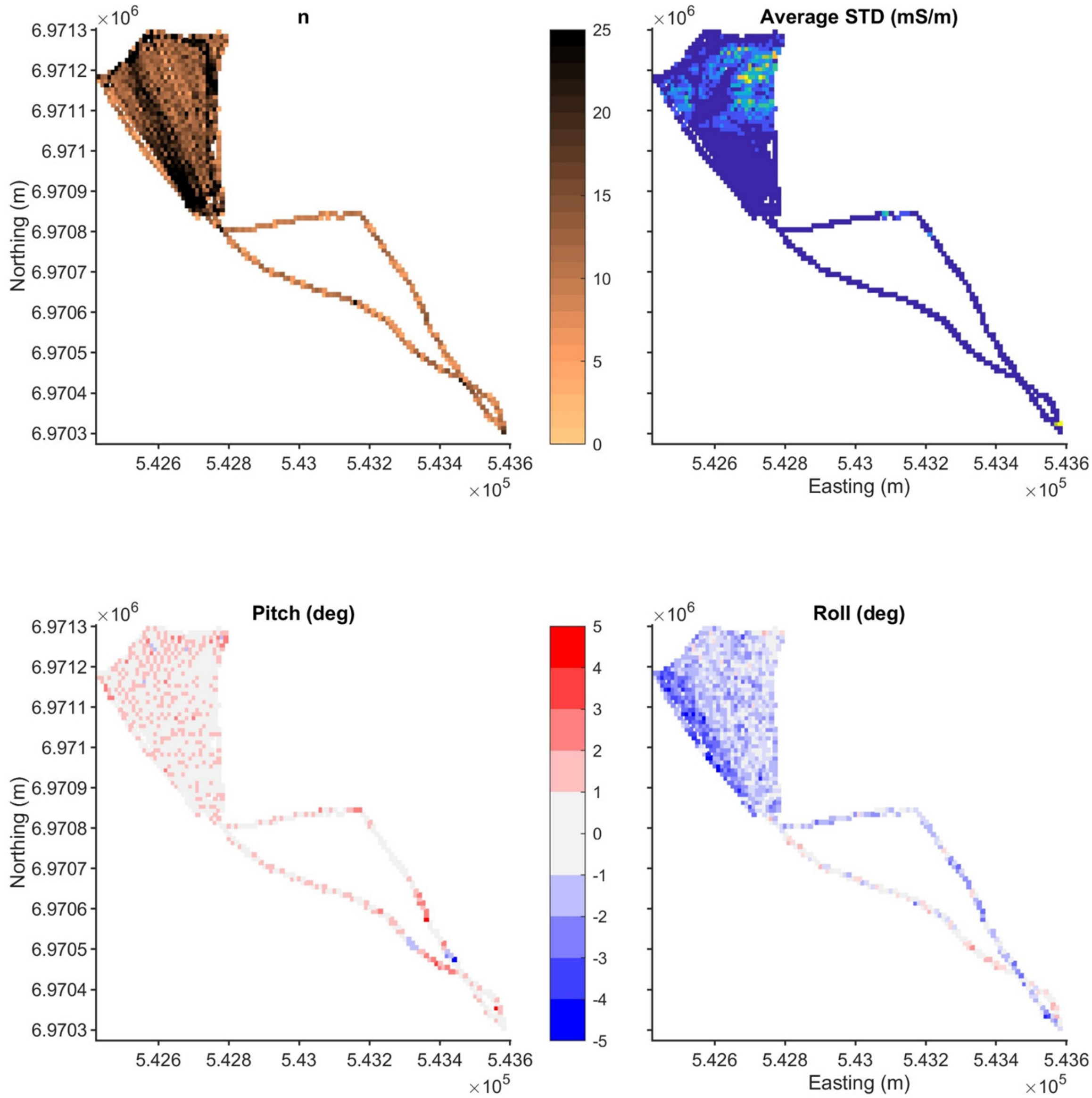


**Figure 5.** Number of observations, average standard deviation of apparent electrical conductivity, average pitch, and average roll over a 10m by 10m grid.

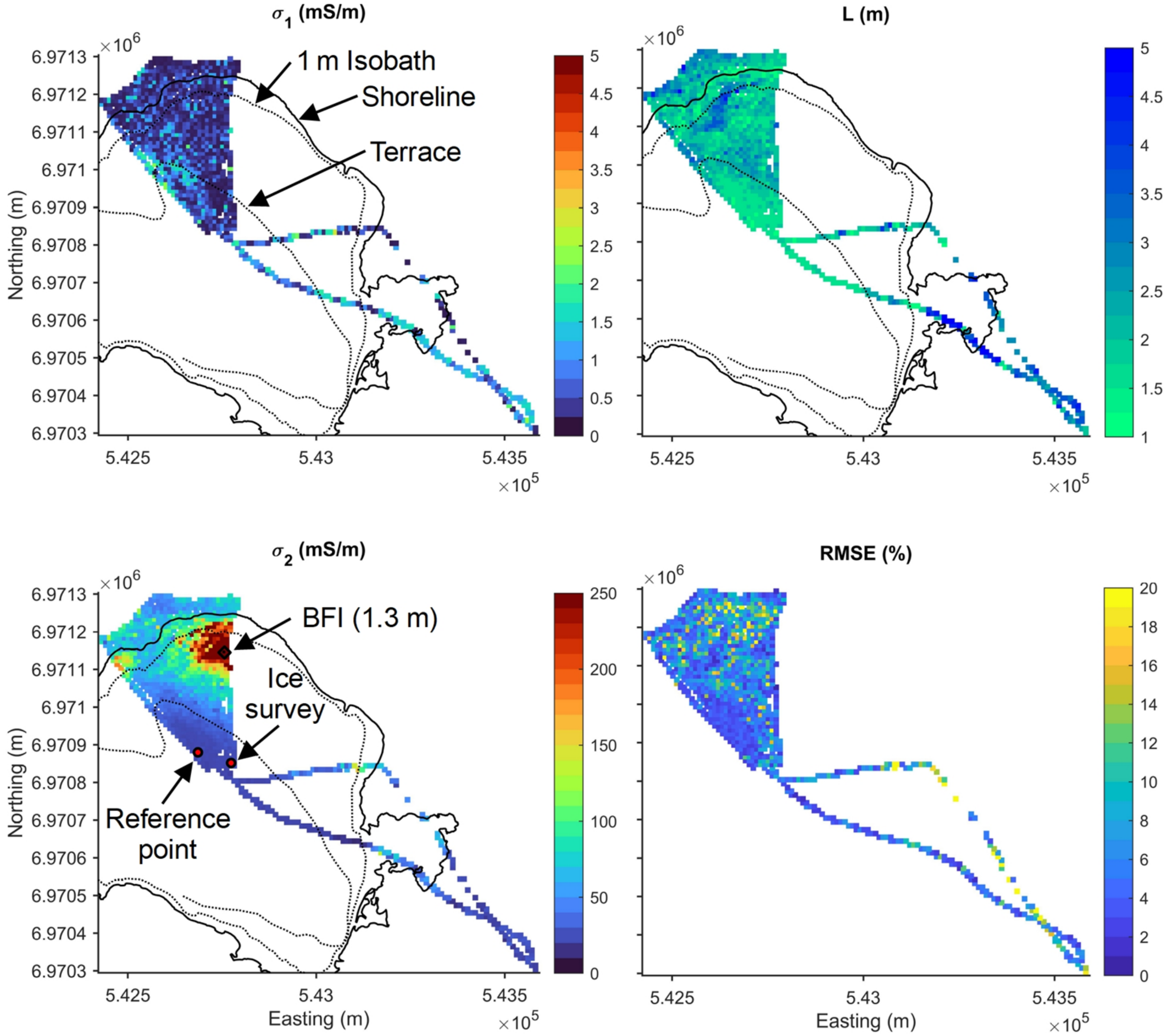


**Figure 6.** Recovered electrical conductivity for an unconstrained two-layer model initialized with an upper layer thickness of 1.7 m, an upper layer conductivity of 1 mS/m, and a lower layer conductivity of $\sigma_{HCP2}$. The average value of $\phi_d$ is 1.6 and the average RMSE is 7.8%. The average recovered upper layer thickness is 2.2 m; the average recovered upper and lower conductivities are 0.5 mS/m and 71 mS/m. The lake shoreline, 1 m isobath, and terrace are shown by the solid, dashed, and dotted black lines.

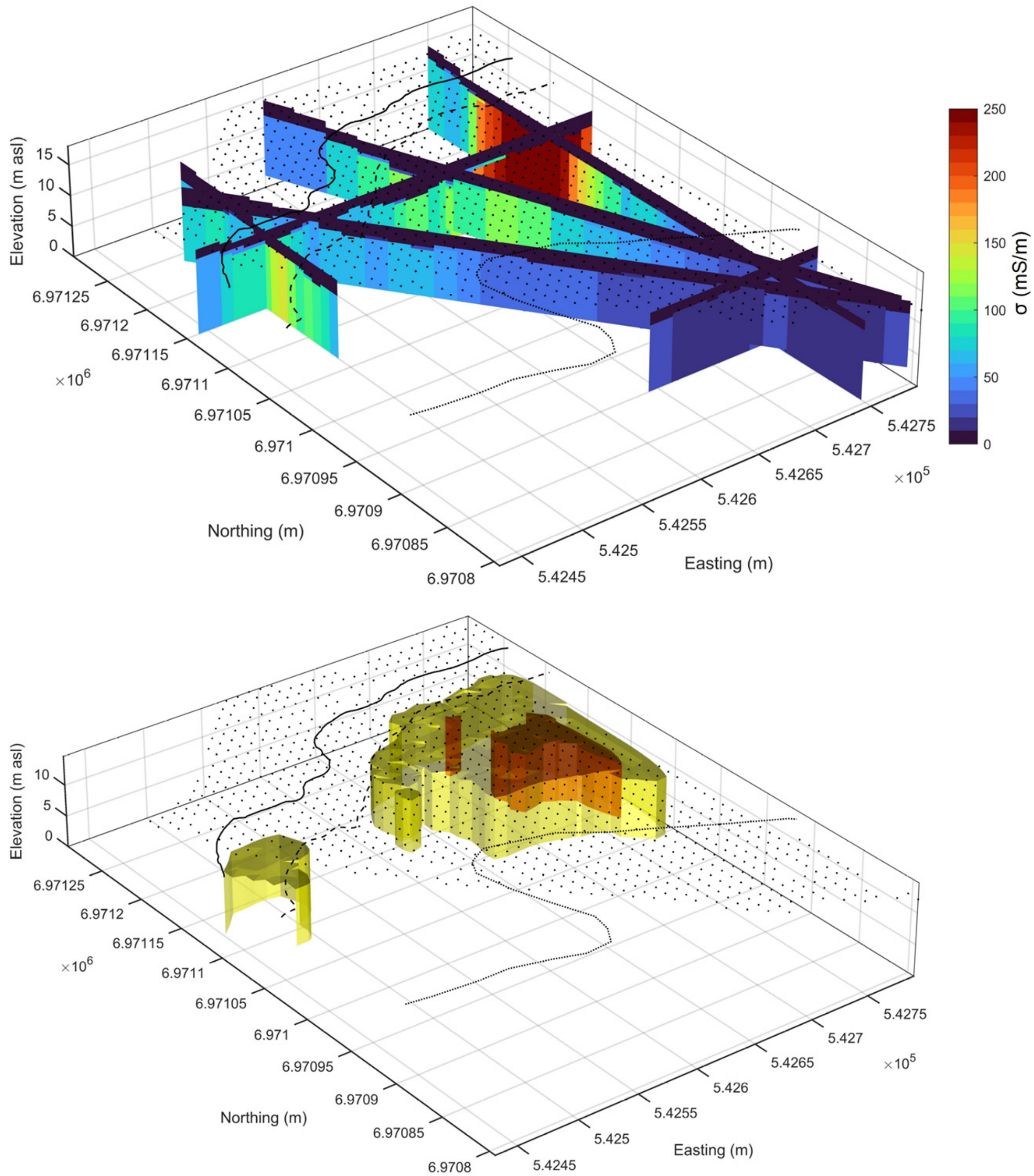


**Figure 7.** Recovered electrical conductivity for the unconstrained two-layer model of Figure 6. The top panel shows the electrical conductivity and the gridded sounding locations. The bottom panel shows isosurfaces of electrical conductivity at 100 mS/m (yellow) and 300 mS/m (red). The lake shoreline, 1 m isobath, and terrace are shown by the solid, dashed, and dotted black lines.

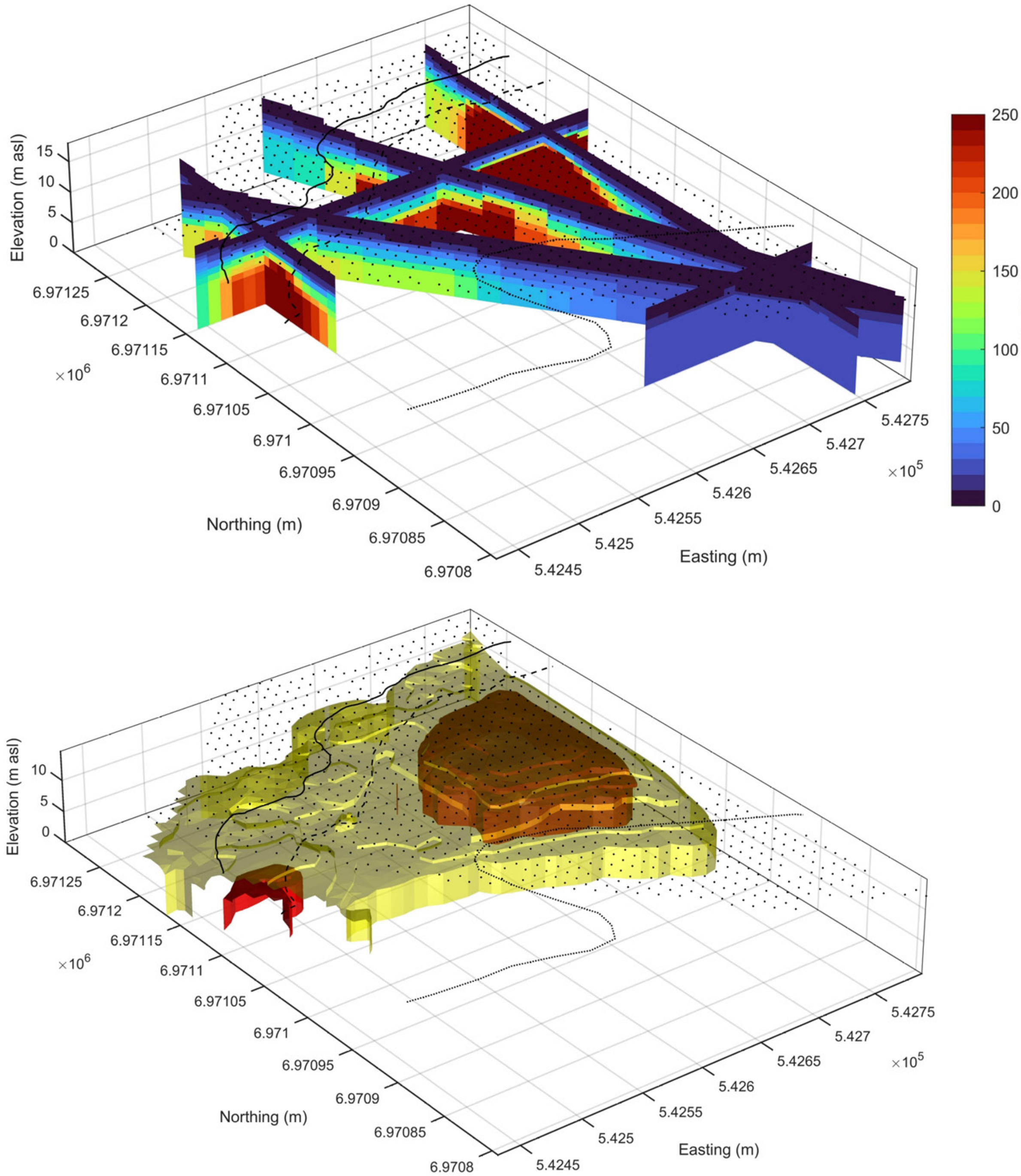


**Figure 8.** Recovered electrical conductivity for a smoothness constrained ten-layer model ($\beta = 5$) initialized with a conductivity of 1 mS/m for the upper 1.7 m of the model ($\alpha = 2$) and a conductivity of $\sigma_{\mathrm{HCP2}}$ for the remaining layers ($\alpha = 0$). The average value of $\phi_d$ is 1.5 and the average RMSE is 9.9%. The bottom panel shows isosurfaces of electrical conductivity at 100 mS/m (yellow) and 300 mS/m (red). The lake shoreline, 1 m isobath, and terrace are shown by the solid, dashed, and dotted black lines.

## APPENDIX A

For a DualEM-42 survey, or other fixed-loop frequency-domain electromagnetic surveys, the measurements consist of in-phase and quadrature secondary magnetic field strength in proportion to the primary field (e.g., Taylor, 1999). The quadrature phase measurements are most sensitive to electrical conductivity and are typically transformed to apparent conductivity using the low-induction number (LIN) approximation (McNeil, 1980). Although the LIN approximation may not always be valid, the data transformation to apparent conductivity does not result in any loss of information, although care must be taken to incorporate any factory- or user-applied height compensation or calibration (e.g., Oldenborger et al., 2020). The in-phase measurements are less sensitive to electrical conductivity, are typically unstable, and are generally not incorporated into inversion for electrical conductivity (e.g., McLachlan et al., 2021).

For quadrature measurements only, the data for a single DualEM-42 sounding consist of apparent conductivity from four channels: $\sigma_{PRP2}$, $\sigma_{PRP4}$, $\sigma_{HCP2}$, and $\sigma_{HCP4}$ (Figure 2). The data are simulated for a one-dimensional earth using the full electromagnetic solution for the magnetic fields that accounts for coil orientation and height above ground (Hanssens et al., 2019b). The simulated secondary quadrature magnetic field strengths are transformed to apparent conductivity (rather than converting the measurements of apparent conductivity to magnetic field strength). All simulations assume free space dielectric permittivity and magnetic permeability (a dielectric constant of unity and a magnetic susceptibility of zero). The data are inverted to recover electrical conductivity by minimizing the least-squares prediction error subject to model constraints as described by objective functions for both the data and the model.

The data objective function is formulated as

$$\psi_d = |\phi_d - 1| \text{where} \phi_d = \frac{1}{N}\sum_{i=1}^{N} [\frac{d_i - f_i(m)}{e_i}]^2$$

where $d_i$ is the apparent conductivity for channel $i$, $f_i(m)$ is the simulated apparent conductivity as a function of the model $m$, $e_i$ is the standard deviation of the $i$th datum, and $N$ is the number of data ($N = 4$ for the DualEM-42). For normally distributed prediction errors, $\phi_d$ takes the form of the reduced chi-squared distribution with an expected value of unity. When $\psi_d$ is minimized to zero, $\phi_d = 1$, and the prediction errors are commensurate with the standard deviation of the data in accordance with the discrepancy principle. In the case that $\psi_d$ cannot be minimized to zero, the value of $\phi_d$ at convergence gives a measure of the sum-squared prediction error relative to the data error. For this study, $e_i$ is estimated by the standard deviation of the grid-based spatial average of apparent conductivity for each channel, but it may be estimated by other means.

The model objective function is formulated as

$\psi_m = \frac{1}{M}\sum_{j=1}^{M}(\alpha_j[\frac{m_j - m_j^r}{m_j^r}]^2 + \beta_j[\frac{d}{dz}\frac{\sigma_j}{\sigma_j^r}]^2 + b_{min}[\frac{\max(0, m^{min} - m_j)}{m_j^r}]^2 + b_{max}[\frac{\max(0, m_j - m^{max})}{m_j^r}]^2)$ where $m^r$ is a reference model, $m^{min}$ is a lower bound model, $m^{max}$ is an upper bound model, and $M$ is the number of model parameters. The weight $\alpha_j$ controls the reference model regularization and the weight $\beta_j$ controls the smoothness regularization for the $j$th layer. The weights $b_{min}$ and $b_{max}$ control the barrier terms for the lower and upper model bounds $m^{min}$ and $m^{max}$. The model $m$ takes one of two forms: 1) a two- or three-layered earth with conductivity-thickness parameter pairs [$\sigma_j$, $L_j$], or 2) a multi-layered earth with more than three layers each of fixed thickness with electrical conductivity $\sigma_j$. In either case, the thickness of the bottom layer is fixed and infinite.

**Case 1**

In the case of a two- or three-layered earth, $M = 3$ or $M = 5$. The total objective function $\psi = \psi_d + \psi_m$ is minimized using Nelder-Mead simplex optimization (Lagarias et al., 1998) with implicit model constraints given by $\psi_m$. Simplex optimization does not require a gradient, and is most suitable when the optimization problem is not smooth, such as when solving simultaneously for layer conductivity and thickness. A two-layer model is initialized with the default reference model of [$\sigma_{HCP2}$, 3.0 m, $\sigma_{HCP4}$, (∞)] and a three-layer model is initialized with the default reference model of [$\sigma_{PRP2}$, 1.0 m, $\sigma_{HCP2}$, 2.0 m, $\sigma_{HCP4}$, (∞)] unless specified otherwise. The default reference, smoothness, and upper bound weights are zero, such that the inversion is (almost) unconstrained. To enforce positivity of electrical conductivity and thickness, the default lower bound is set according to $\sigma_{min} = 0.1$ mS/m, $L_{min} = 0.1$ m, and $b_{min} = 10^4$. For a two-layer model, the unconstrained inversion is strictly overdetermined, although imperfect or redundant data may require the use of constraints to obtain a stable solution. A three-layer unconstrained model is strictly underdetermined and practice shows that a stable model cannot be recovered without application of significant constraints.

**Case 2**

In the case of a multi-layer earth, layers are specified and $M$ is equal to the number of layers, including the bottom layer. The total objective function $\psi = \psi_d + \psi_m$ is minimized using quasi-Newton optimization (Nocedal and Wright, 2006) with finite-difference calculation of the gradient, and implicit model constraints given by $\psi_m$. The model is initialized with the default homogeneous reference model of [$\sigma_{HCP2}$] unless specified otherwise, and the default reference and smoothness regularization weights are zero. For the multi-layer case, the model is log-transformed to $m_j = \ln(\sigma_j)$ which results in improved performance of the quasi-Newton optimization. In this case, the terms in the model objective function are *not* normalized by the reference model since the log transform is unitless and accounts for scaling without the need for normalization. The log transform also enforces positivity and the default barrier weights are set to zero. For the multi-layer model, the unconstrained inversion is strictly underdetermined and practice shows that a stable model cannot be recovered without application of smoothness and/or reference regularization.

In either case of model parameterization, the inversion algorithm does not account for the non-monotonic behaviour of the quadrature secondary magnetic field as a function of ground conductivity (e.g., Hanssens et al., 2019a; McLachlan et al., 2021). This shortcoming imparts a reduced sensitivity followed by an inherent non-uniqueness to the forward modelling component of the inversion for electrical conductivity in excess of approximately 1000 mS/m for the HCP4 channel of the DualEM-42. For these high conductivity environments, the inversion may find a valid local minimum of the objective function on either side of the quadrature-conductivity maximum (regardless of non-uniqueness introduced by noise and over-parameterization of the model). For the given algorithm, this shortcoming may be overcome by using an appropriate reference and/or initial model.

**Synthetic Example**

A simple two-layer synthetic model with variable layer thickness is illustrated in Figure A1. The model is comprised of a low conductivity layer over a more conductive substrate. The simulated apparent conductivity data clearly reflect the model characteristics, if not the true electrical conductivity and geometry. Results of an unconstrained two-layer inversion are shown in Figure A2 and results of an initialized two-layer inversion are shown in Figure A3. When completely unconstrained, the inversion is able to recover a two-layer model reasonably well, although there is some trade-off between conductivity and layer thickness as is well recognized for inversion of electromagnetic data (Figure A2). When the upper layer is initialized to 1 mS/m, the recovered model is more accurate in terms of electrical conductivity and layer thickness (Figure A3). Both models fit the data equally well, illustrating the inherent non-uniqueness of the problem due to data redundancy—the data are not totally independent in terms of sensitivity to the model. Model space can be further constrained by the addition of a reference model, or by the application of model smoothness (although smoothness is not necessarily compatible with a layered model inversion).

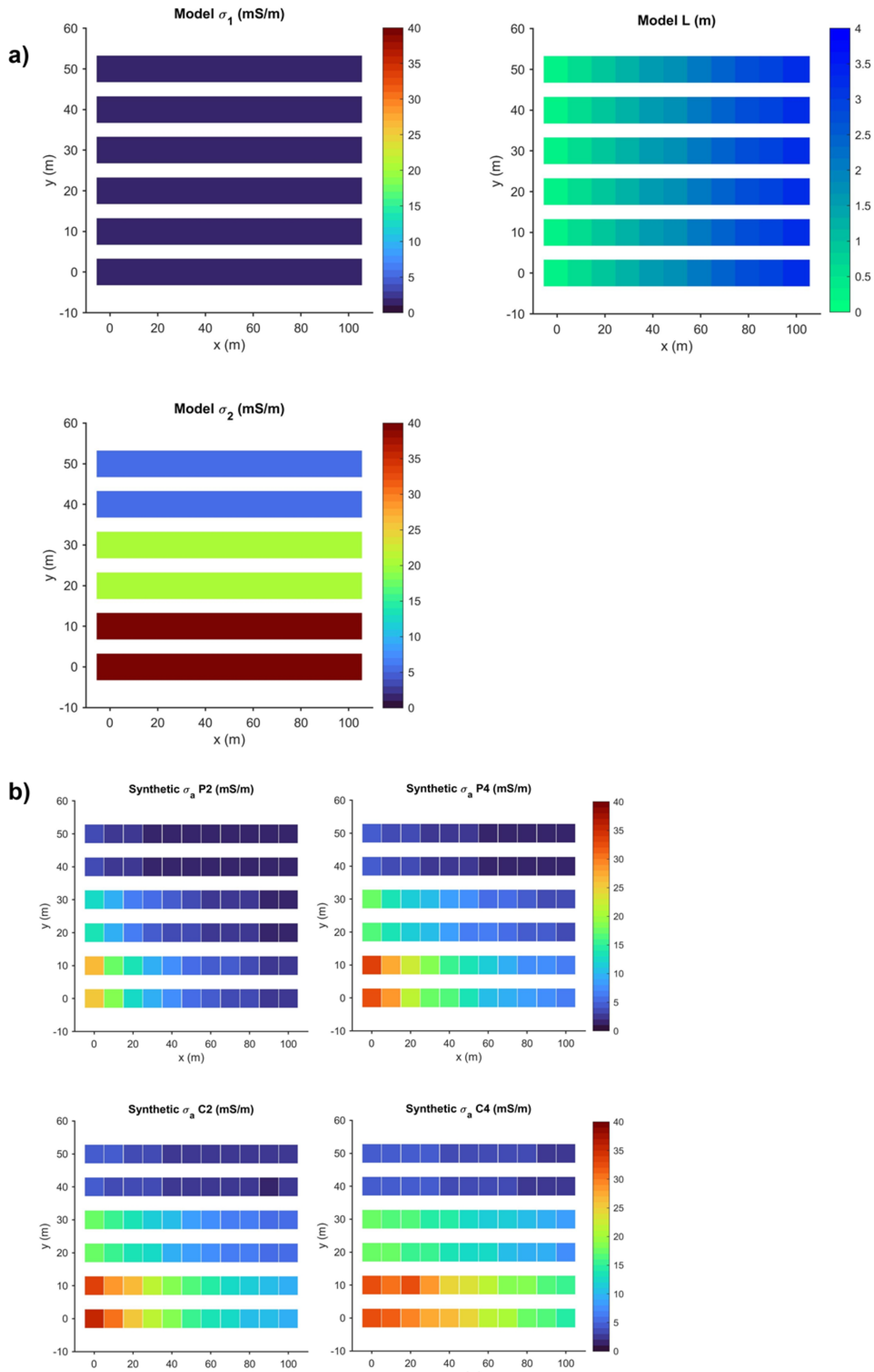


**Figure A1.** a) Synthetic two-layer model with upper layer conductivity $\sigma_1$, lower layer conductivity $\sigma_2$, and upper layer thickness $L$. b) Simulated apparent conductivity as measured by a DualEM-42 at 0.1 m height with the addition of 3% normally distributed random noise.

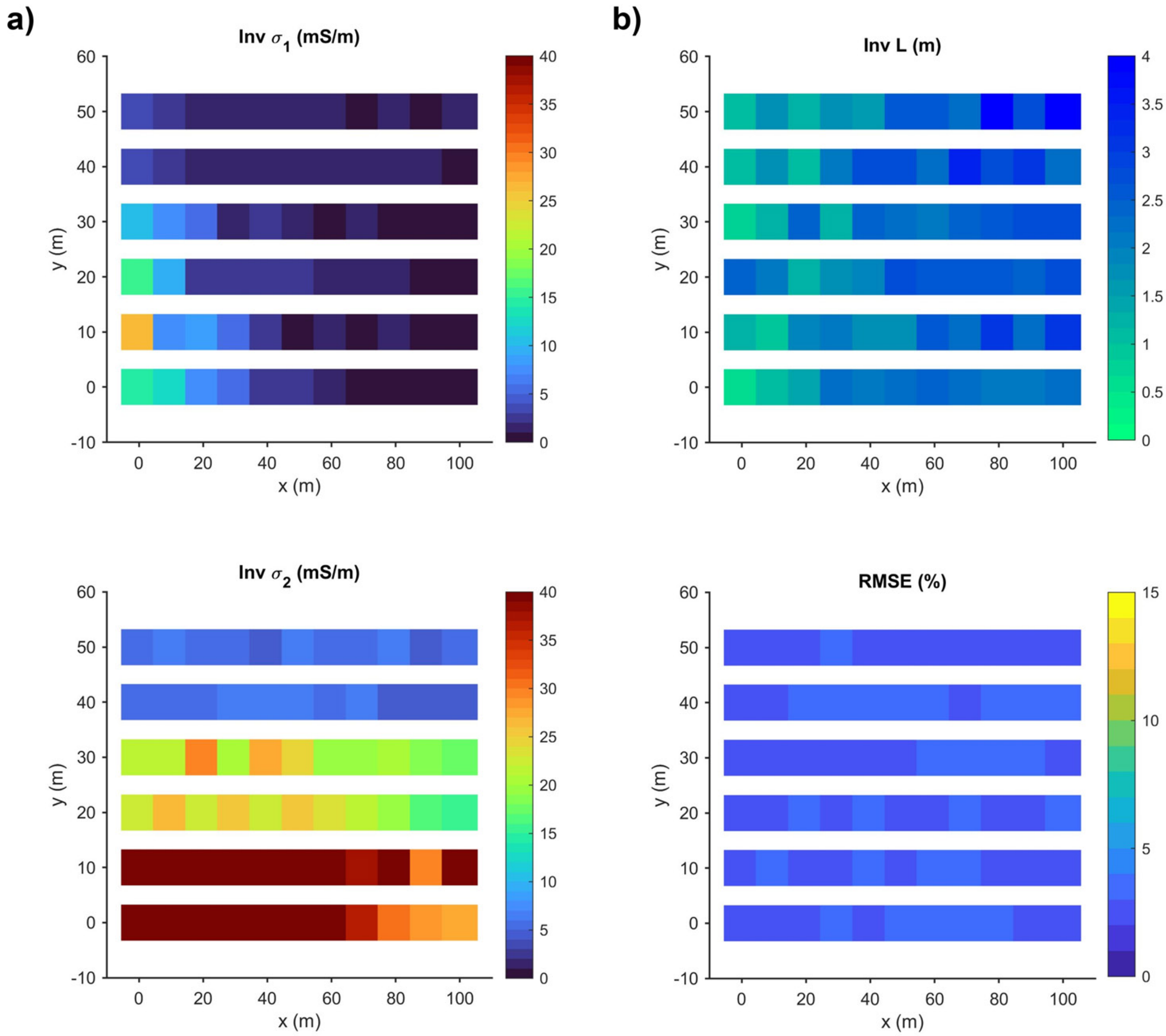


**Figure A2.** a) Recovered electrical conductivity for the simulated noisy data in Figure A1 using an unconstrained two-layer inversion with the default initial model (see Appendix). b) Recovered layer thickness and RMSE. The average value of $\phi_d$ is 1.0 and the average RMSE is 3%, commensurate with data noise.

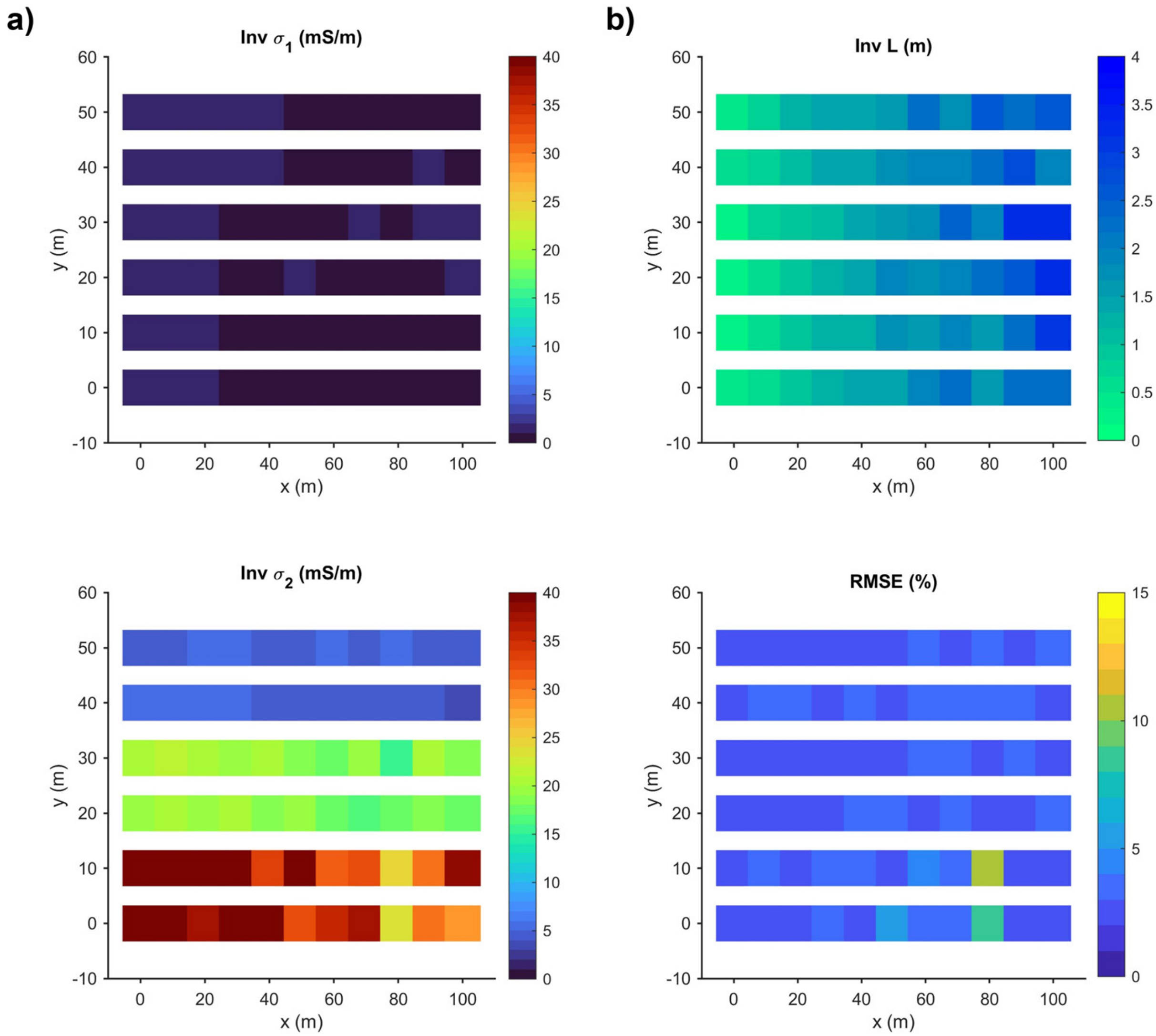


**Figure A3.** a) Recovered electrical conductivity for the simulated noisy data in Figure A1 using an unconstrained two-layer inversion with the initial upper layer conductivity set to 1 mS/m. b) Recovered layer thickness and RMSE. The average value of $\phi_d$ is 1.0 and the average RMSE is 3%, commensurate with data noise.